applied sciences

MDPI

Article

Mechanism and Parametric Study on Pullout Failure of Tunnel Anchorage in Suspension Bridges

Menglong Dong [1,*], Zhijin Shen [2], Xiaojie Geng [2], Li Zhang [2] and Aipeng Tang [2]

[1] School of Earth Science and Engineering, Hohai University, Nanjing 210098, China
[2] Changjiang Survey, Planning, Design and Research Co., Ltd., Wuhan 430010, China; zhangli8@cjwsjy.com.cn (L.Z.); tangaipeng@cjwsjy.com.cn (A.T.)
* Correspondence: dongml@hhu.edu.cn; Tel.: +86-13914484280

Abstract

Tunnel anchorages are critical components in long-span suspension bridges, transferring immense cable forces into the surrounding rock mass. Although previous studies have advanced the understanding of their pullout behavior through field tests, laboratory models, numerical simulations, and theoretical analyses, significant challenges remain in predicting their performance in complex geological conditions. This study investigates the pullout failure mechanism and bearing behavior of tunnel anchorages situated in heterogeneous conglomerate rock, with application to the Wujiagang Yangtze River Bridge in China to employ a tunnel anchorage in such strata. An integrated research methodology is adopted, combining in situ and laboratory geotechnical testing, a highly instrumented 1:12 scaled field model test, and detailed three-dimensional numerical modeling. The experimental program characterizes the strength and deformation properties of the rock, while the field test captures the mechanical response under design, overload, and ultimate failure conditions. Numerical models, calibrated against experimental results, are employed to analyze the influence of key parameters such as burial depth, inclination, and overburden strength. Furthermore, the long-term stability and creep behavior of the anchorage are evaluated. The results reveal the deformation characteristics, failure mode, and ultimate pullout capacity specific to weakly cemented and stratified rock. The study provides novel insights into the rock–anchorage interaction mechanism under these challenging conditions and validates the feasibility of tunnel anchorages in complex geology. The findings offer practical guidance for the design and construction of future tunnel anchorages in similar settings, ensuring both safety and economic efficiency.

Keywords: tunnel anchorage; pullout failure mechanism; scaled model test; numerical simulation; heterogeneous rock; bearing capacity; long-term stability

check for updates

Received: 4 October 2025
Revised: 23 October 2025
Accepted: 28 October 2025
Published: 30 October 2025

Citation: Dong, M.; Shen, Z.; Geng, X.; Zhang, L.; Tang, A. Mechanism and Parametric Study on Pullout Failure of Tunnel Anchorage in Suspension Bridges. *Appl. Sci.* **2025**, *15*, 11587. https://doi.org/10.3390/app152111587

Copyright: © 2025 by the authors. Licensee MDPI, Basel, Switzerland. This article is an open access article distributed under the terms and conditions of the Creative Commons Attribution (CC BY) license (https://creativecommons.org/licenses/by/4.0/).

1. Introduction

Suspension bridges are widely recognized as one of the most efficient structural forms for long-span crossings due to their excellent material utilization, esthetic appeal, minimal environmental disruption, and reduced need for large-scale foundation works. The main load-bearing components of a suspension bridge include the main cables, towers, stiffening girders, and anchorages [1–3]. Based on the cable anchoring method, suspension bridges can be categorized into self-anchored and ground-anchored types. While self-anchored systems anchor the main cables directly to the stiffening girders, introducing significant axial compression that limits their applicability to moderate spans, ground-anchored

systems transmit cable forces into the foundation rock or soil via anchor blocks, making them more suitable for long-span bridges [4].

As a critical load-transfer component in ground-anchored suspension bridges, the anchorage accounts for 30–40% of the total bridge cost. Tunnel anchorages, which leverage the surrounding rock mass to resist tensile forces through a wedge-shaped mechanism, offer economic and construction advantages compared to gravity anchorages, especially in suitable geological conditions [5]. However, the bearing behavior and failure mechanisms of tunnel anchorages are complex and influenced significantly by rock–structure interaction, which remains inadequately understood—particularly in heterogeneous rock formations [6–8].

Previous research has combined field and laboratory model tests, theoretical analyses, and numerical simulations to investigate the pullout behavior and bearing capacity of tunnel anchorages [9,10]. Field tests, such as those conducted for the Humen Bridge, Balinghe Bridge, and E'gongyan Bridge, have provided valuable insights into deformation characteristics and failure modes. Laboratory physical modeling has further enabled the study of failure mechanisms and parametric influences under controlled conditions [11,12]. Numerical simulations have complemented these efforts by offering detailed stress and deformation analyses [13,14].

Despite these advances, significant challenges remain. Field and laboratory tests are often constrained by scale effects, material similitude limitations, and site-specific conditions. The long-term creep behavior and stability of tunnel anchorages under sustained loading require further investigation. Due to the inherent limitations of the aforementioned physical model tests, there remains a critical gap in the understanding of the long-term creep behavior and stability of tunnel anchors, a complex geotechnical structural system, under sustained loading. Physical model tests struggle to simulate time effects spanning decades or even centuries, while limitations in material similarity make it particularly challenging to accurately replicate the intrinsic creep characteristics of both the surrounding rock and structural materials. Consequently, findings from physical experiments must be supplemented and extended through numerical simulations and theoretical analyses that adequately account for time-dependent effects and real material properties.

Tunnel anchorages function by mobilizing the surrounding rock mass through a wedge-shaped plug effect, significantly enhancing the pullout resistance. This mechanism is efficient but highly dependent on geological conditions. In challenging environments such as soft or stratified rock, predicting the failure mode and ensuring long-term stability become complicated. Existing studies have employed reduced-scale field tests and geotechnical centrifuge modeling to simulate anchorage behavior. However, these methods often fail to fully replicate the overburden pressure and stratigraphic variability. Numerical models offer an alternative but require validation against high-quality experimental data.

Wu et al. conducted large-scale field model tests to investigate the mechanical behavior of rock mass around tunnel anchorages under different loading conditions, and evaluated the potential bearing capacity of tunnel anchorages for a proposed super-large railway suspension bridge based on practical engineering cases [15]. Based on field model tests, Han et al. systematically analyzed the bearing performance of tunnel anchorages in soft rock with weak interlayers, categorized the deformation stages of the surrounding rock, and identified that the ultimate failure mode under specific geological conditions resembles an inverted wedge [16,17]. Furthermore, some scholars determined the bearing capacity of tunnel anchorages under various rock mass conditions by analyzing monitoring data from field model tests, providing valuable references for the actual construction of suspension bridges. Shen et al. performed design load tests, overload tests, failure tests, and rheological tests on a 1:12 full-scale field model. The results indicated that when the test load exceeded

the overload stability coefficient, a distinct inflection point appeared in the deformation curve; whereas when the load was below this threshold, both deformation and rheological characteristics of the anchorage were negligible [18].

However, scaled field model tests are often constrained by loading conditions, making it difficult to accurately simulate the failure state of the surrounding rock. As a result, it remains challenging to fully understand the failure mode and uplift process of the rock in the anchorage zone, or to determine the ultimate bearing capacity of the tunnel anchorage. To address these limitations, researchers have improved in situ scaled model tests by considering the rock mass characteristics and instrument capabilities at the test site. In this context, indoor physical model tests have emerged as an effective alternative for simulating rock failure conditions, offering further insights into the failure mechanisms of surrounding rock and the collaborative working mechanism of the "tunnel anchorage–surrounding rock" system.

Regarding indoor model tests, scholars have conducted in-depth research on the interaction mechanism between tunnel anchorages and surrounding rock, as well as structural optimization. By varying parameters such as the embedment depth of the anchorage body and rock mass conditions, they systematically examined the stress-deformation behavior of the tunnel anchorage and surrounding rock, the load-transfer mechanism and bearing capacity of the anchorage structure, and the deformation patterns of the rock mass. Lim and Seo carried out pullout tests on tunnel anchorages using indoor models. Based on experimental phenomena and data, they clarified the factors influencing failure and further explored the failure modes and bearing capacity of tunnel anchorages [19–21].

Xia et al. employed two-dimensional particle flow numerical simulation to study the effects of structural plane dip angles and confining pressure on the failure characteristics, mechanical response, and slip behavior of rock masses [22]. Liang et al. combined model testing with numerical analysis to investigate the deformation evolution of surrounding rock during adjacent construction, focusing particularly on the influence of the distance between the anchorage and adjacent tunnels, as well as the effect of tunnel burial depth on anchorage deformation [23]. Zhou et al. conducted a case study on the tunnel anchorage of a long-span suspension bridge using three-dimensional numerical simulation to examine the impact of adjacent tunnel excavation on anchorage stability [24]. Zhang et al. developed a refined numerical model to analyze the load-response behavior of a railway suspension bridge tunnel anchorage embedded in fractured rock interlayers. Through a comprehensive stability assessment, they verified the applicability and safety of such anchorages under complex geological conditions [25]. Ko et al. validated the effectiveness of a numerical model by comparing finite element simulation results with data from small-scale model tests of tunnel anchorages, demonstrating good agreement between numerical predictions and experimental results. These studies collectively provide a theoretical foundation for the broader application of tunnel anchorage technology [26]. Furthermore, Thirukumaran et al. proposed using the interface shear stiffness as a criterion for evaluating anchorage quality, based on a comparative analysis of pullout tests and numerical simulations [27]. Sahoo et al. incorporated seismic factors into the stability analysis of tunnel anchorage systems, employing numerical analysis methods in their study [28].

Previous studies have enhanced the understanding of tunnel anchorage behavior through various approaches, including field tests (providing critical data on deformation and ultimate bearing capacity), laboratory model tests (simulating failure propagation using analogous materials), and numerical simulations (analyzing rock–anchor interaction via finite element and finite difference methods). However, significant limitations remain: physical models struggle to accurately represent geological heterogeneity, scale effects often

distort stress and deformation fields, and research on the creep behavior and long-term performance of anchorages under high sustained loads remains relatively limited.

The Wujiagang Bridge site features unevenly cemented conglomerate with interlayers of sandstone, presenting a unique opportunity to study tunnel anchorage behavior in non-uniform rock. Understanding the pullout mechanism in such contexts is essential for optimizing design and ensuring safety. This study focuses on the tunnel anchorage of the Wujiagang Yangtze River Bridge—the first of its kind in conglomerate strata in China. Combining in situ testing, laboratory experiments, physical modeling, and numerical simulations, we aim to elucidate the pullout mechanism, failure modes, and long-term performance of tunnel anchorages in complex geological conditions. The research outcomes are expected to provide theoretical and practical guidance for the design and construction of tunnel anchorages in similar settings.

2. Research Background

2.1. Project Overview

This paper presents the Wujiagang Yangtze River Bridge in China as a case study. As a suspension bridge, its main span incorporates a tunnel anchorage system on the north bank, capitalizing on a stable "rock hill" near the bridge approach. The anchorage is directly embedded into the intact rock mass (see Figure 1), eliminating the need for extensive foundation pits or river terrace support structures. This design achieves an optimal balance between environmental sustainability and cost-effectiveness. The tunnel anchorage is designed as a twin-tunnel system with an axial length of 45 m and a tilt angle of 40°. The anchorage body adopts a wedge-shaped geometry, gradually expanding from a narrower front face (9.0 m × 11.4 m) to a broader rear face (16.0 m × 20.0 m). The minimum clear spacing between the twin anchors measures approximately 23.42 m (refer to Figure 2 for detailed dimensions).

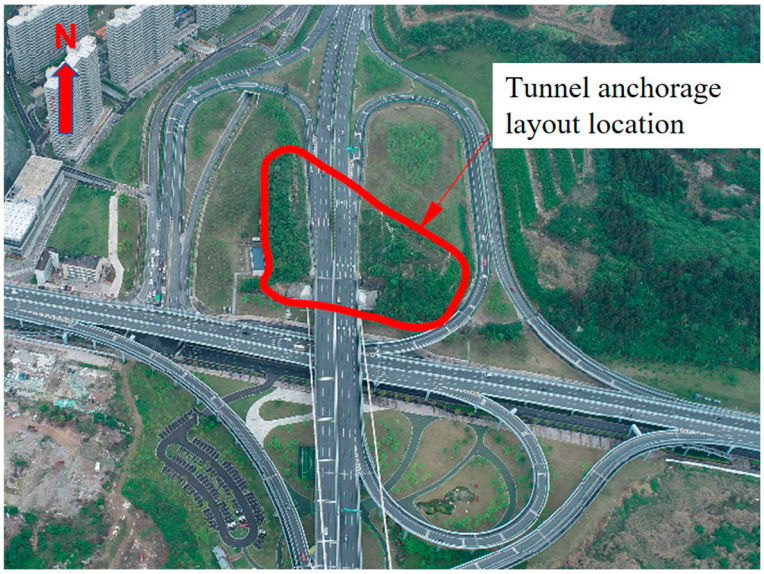


Figure 1. Field Photo of the Tunnel Anchorage Location.

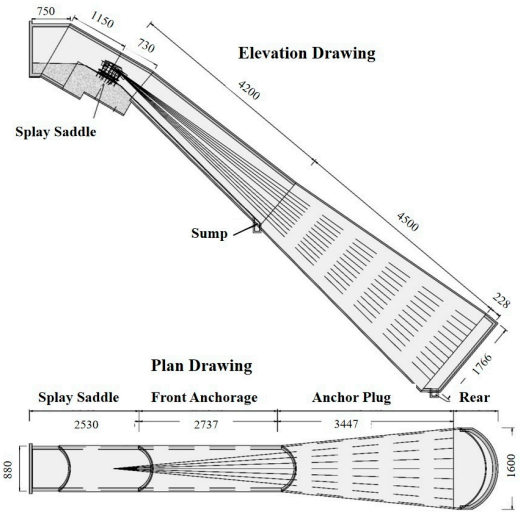


Figure 2. Structural Schematic of the Tunnel Anchorage (cm).

2.2. Physical and Mechanical Parameters of Rock

A comprehensive series of laboratory tests was conducted on representative rock samples from the anchor zone, including physical property tests, uniaxial compression tests, tensile tests, direct shear tests, triaxial compression tests, and triaxial creep tests. Additionally, deformation tests, direct shear tests, rock–concrete interface shear tests, and concrete pullout tests were performed on representative rock masses. Based on the test results, geological generalization and rock mass quality evaluation were carried out. Samples of typical conglomerate and sandy conglomerate were collected from each member of the Luojingtan Formation for testing. The experimental program comprised: 19 sets of rock physical property tests, 16 sets of rock uniaxial compression, tensile, and deformation tests, 8 sets of triaxial compression tests, and 4 sets of direct shear tests. The test results are presented in Tables 1–3. Analysis of the direct shear test results demonstrated that the derived shear strength parameters were lower than those obtained from triaxial compression tests, confirming that confining pressure significantly enhances rock shear strength.

Table 1. Results of rock physical parameters.

Stratum	Lithology	Degree of Weathering	Density (g/cm^3)			Water Content (%)	Water Absorption (%)	Porosity (%)
			Dry	Bulk	Saturated			
K_2l^2	Sandy conglomerate	Medium	2.25	2.29	2.41	1.69	7.14	12.3
		Slightly	2.60	2.60	2.60	0.80	1.90	5.04
	Conglomerate	Slightly	2.50	2.50	2.60	0.70	3.30	8.34
K_2l^1	Conglomerate	Slightly	2.60	2.60	2.60	0.60	1.90	4.94
K_2l^2	Sandstone interlayer	Medium	2.40	2.50	2.50	0.80	4.40	9.90

Table 2. Mechanical parameters of rock—uniaxial tests.

Stratum	Lithology	Degree of Weathering	Uniaxial Compressive Strength (MPa)		Softening Coefficient	Poisson's Ratio		Tensile Strength (MPa)
			Bulk	Saturated		Bulk	Saturated	
K_2l^2	Sandy conglomerate	Medium	12.7	5.49	0.43	0.27	0.29	0.42
		Slightly	25.4	12.4	0.49	0.26	0.28	0.50
	Conglomerate	Slightly	28.3	12.8	0.45	0.26	0.27	0.92
K_2l^1	Conglomerate	Slightly	29.7	17.4	0.59	0.25	0.27	1.01
K_2l^2	Sandstone interlayer	Medium	11.0	5.13	0.47	0.27	0.28	0.40

Table 3. Results of rock triaxial compression tests.

Stratum	Lithology	Degree of Weathering	f	φ (°)	Cohesion (MPa)
K_2l^2	Sandy conglomerate	Medium	0.82	39.4	5.53
K_2l^1	Conglomerate	Slightly	1.03	45.8	6.94
K_2l^2	Conglomerate	Medium	0.95	43.5	5.15
K_2l^1	Sandstone interlayer	Slightly	1.16	49.2	5.52

3. Field Scale-Down Test

The pullout resistance of tunnel anchors is highly dependent on the lithological properties of the surrounding rock. In this study, a suitable test site was selected within the research area, where the stratigraphic lithology closely resembles that of the actual geological formation. A 1:12 scaled-down field model test was conducted, accounting for on-site construction constraints. The chosen site offers an open space that accommodates large equipment, enabling the use of a relatively large-scale model to reduce size effect interference. Furthermore, the natural terrain was strategically utilized to improve topographic similarity between the scaled model and real-world conditions.

3.1. Experimental Design and Physical Model Construction

Given the spatial constraints and testing limitations at the actual site, a geometric scaling ratio of 1:12 was adopted for the experimental setup. Based on the in situ geological conditions and the constraints of instrument construction, we ultimately determined an on-site scaling ratio of 1:12. In accordance with similarity theory principles, while maintaining identical material properties and disregarding body forces, the strength and elastic modulus maintain a 1:1 ratio between prototype and model. However, the load scaling follows a 1:144 ratio (derived from 12^2). Through comprehensive analysis of topographical features and lithological conditions, the model test site was strategically located on a relatively open and level platform north of the tunnel anchor hillside. To ensure enhanced topographical fidelity, the scaled model incorporated not only geometric proportionality but also artificial excavation techniques to accurately replicate the actual terrain configuration, as illustrated in Figure 3.

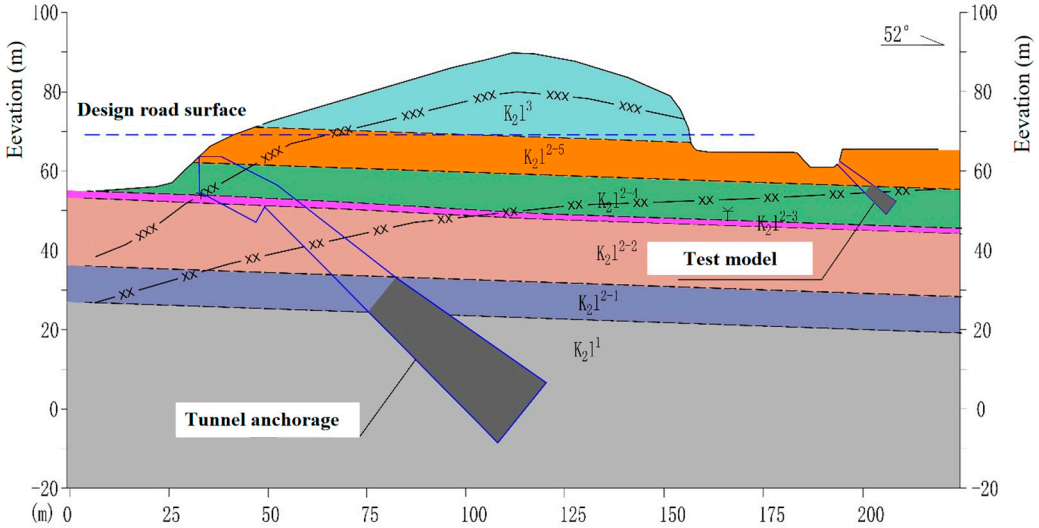


Figure 3. Comparison of Topographic Similarity Between Scaled-Down Model Test and Actual Terrain.

Field investigations revealed that the first member of the Luojingtan Formation (K_2l^1), which corresponds to the prototype anchor location, was deeply buried and thus inaccessible for testing. As an alternative, the upper rock mass of the third member (K_2l^3) was selected as the test stratum due to its comparable lithology, including characteristic sandstone interbeds, matching the actual geological formation. To evaluate the equivalent rock mass quality of the model anchor site, the crosshole seismic wave testing method was employed. The measured P-wave velocity ranged from 3500 to 4300 m/s (average: 3900 m/s), which indicates favorable rock mass integrity. This range shows a high degree of consistency with the P-wave velocity range of the prototype anchor site (4000 to 4200 m/s). This key data not only validates the similarity in dynamic characteristics of the rock mass between our physical model and the prototype but also indirectly demonstrates that the model anchor site successfully replicates the favorable rock mass quality and integrity of the original site. Furthermore, the rock mass integrity surrounding the model anchor is highly consistent with that of the actual bridge anchor, ensuring representative test conditions.

Based on test results from three sample groups in the conglomerate (K_2l^2) where the model anchor is situated, the average saturated uniaxial compressive strength was measured at 15.6 MPa, demonstrating fundamental consistency with the load-bearing surrounding rock strength of the actual bridge-tunnel anchor.

The anchor model was precision-manufactured at a 1:12 geometric scale, with all cavity dimensions rigorously maintaining similarity principles. Key dimensional parameters, referenced to the rear anchor face, include: Burial depth is 6.7 m, axial spacing is 2.5 m, and anchor length is 3.75 m. The model anchor maintains a 40° inclination angle from horizontal, precisely replicating the installation geometry of the prototype bridge anchor.

The anchor body was constructed using reinforced C40 concrete, incorporating five longitudinal steel bars and transverse stirrups, all composed of φ10 mm ribbed reinforcement. The experimental setup employed the push-back method, utilizing the rear rock mass as a reaction structure. The loading system consisted of eight hydraulic jacks, each capable of applying a maximum load of 2000 tons (equivalent to 13 times the design load). To ensure uniform load distribution, 50 cm and 30 cm thick reinforced concrete reaction plates-reinforced with ribbed steel bars-were cast at the front and rear ends of the jacks, respectively.

The cyclic loading test protocol implemented a controlled staged loading-unloading sequence, where the single design load was applied progressively through five complete load cycles before complete unloading to baseline conditions. Measurement procedures consisted of immediate readings upon each load application followed by periodic measurements at 10 min intervals, with load-stage advancement permitted only when consecutive readings demonstrated deformation variations below the 0.002 mm stabilization threshold. This identical measurement protocol and stabilization criterion were rigorously maintained throughout both loading and unloading phases to ensure consistent data collection.

The experimental program included overload testing at 3.5P (3.5 times design load) and 7P (7 times design load) levels. The loading protocol consisted of incremental application in 5–7 stages, with the specific number adapted to test conditions. Load stabilization was confirmed when consecutive measurements (recorded at 20 min intervals) showed displacement variations below 0.002 mm. Unloading was systematically conducted in 5 discrete stages. For the failure test, the design load was progressively increased until either structural failure occurred or the system reached the hydraulic jacks' maximum capacity (2000 tons).

3.2. Surrounding Rock Deformation Analysis

The displacement monitoring results revealed a pronounced increase in free surface deformation with progressive load increments, as illustrated in Figure 4a. Under a 1P load, the maximum deformation measured 0.046 mm. This value escalated to 0.158 mm at 3.5P and further surged to 0.509 mm under 7P loading. The data demonstrates a clear trend of accelerated deformation rates under higher load conditions.

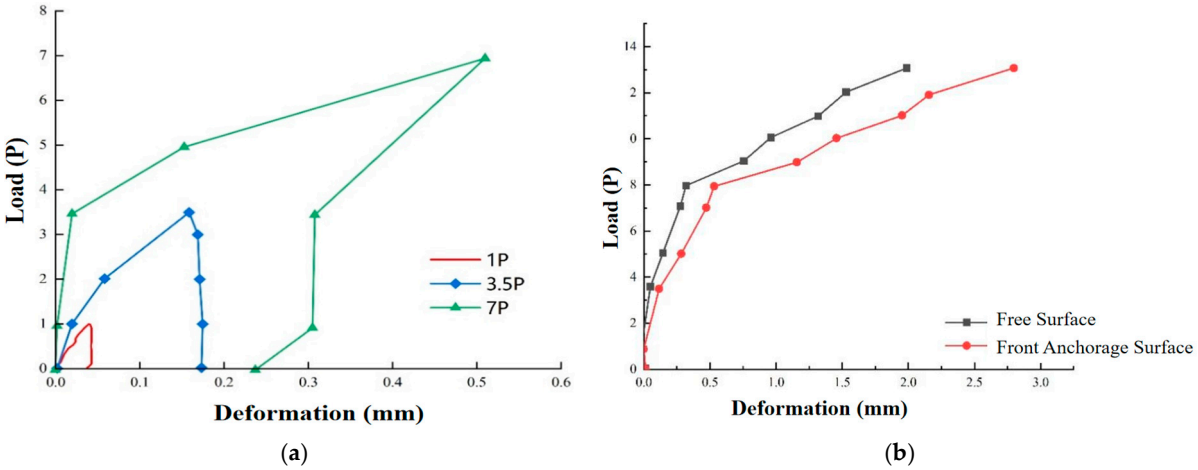


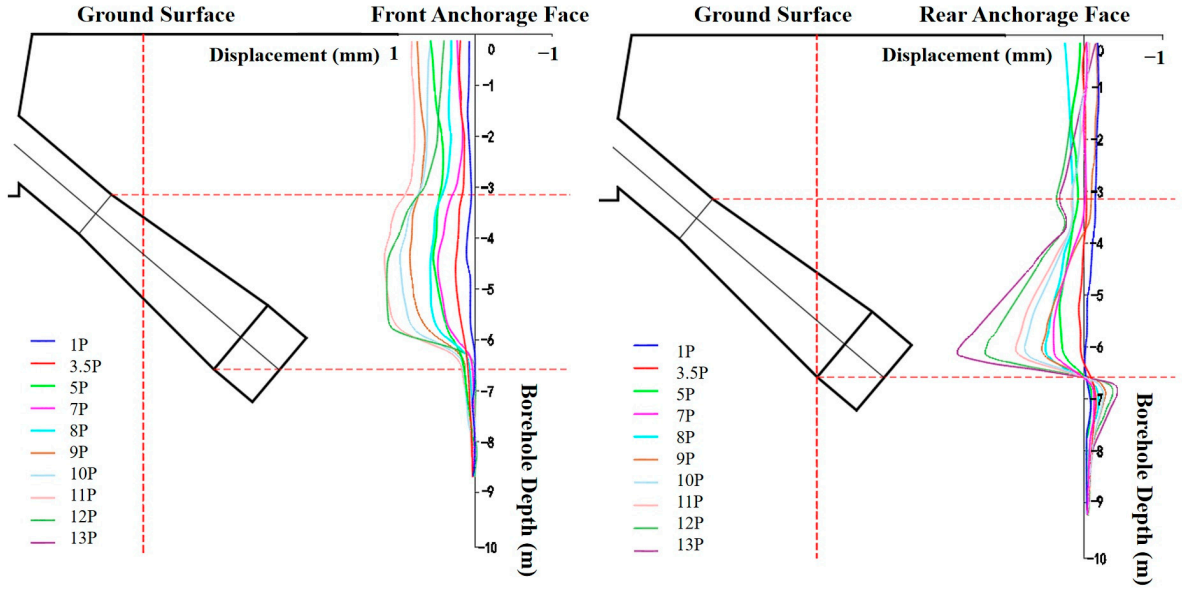
Figure 4. Deformation of model test. (**a**) Deformation of the surrounding rock free surface; (**b**) Deformation of inter-anchor surrounding rock under graded loading.

The surrounding rock between adjacent anchors demonstrates negligible horizontal deformation beneath the anchorage zone. Within the 3.0–6.5 m borehole depth interval, the front anchorage face exhibits pronounced horizontal dislocation. Notably, the overlying rock mass (above 3.0 m depth) manifests backward-inclined deformation, with the associated horizontal dislocation zone spanning approximately twice the anchor body width. Furthermore, the rear anchorage face displays coherent horizontal deformation propagating continuously from the anchorage zone to the surface rock mass.

Under graded loading conditions, the anchorage surrounding rock demonstrates predominantly axial deformation. The deformation characteristics of the free surface, front anchorage face, and inter-anchor rock mass consistently follow this trend, maintaining remarkable stability. In contrast, the rear anchorage face exhibits more complex deformation

behavior. Of particular significance is the dramatic escalation in deformation observed in the inter-anchor rock mass when the applied load exceeds 8P, as clearly illustrated in Figure 4b.

The rupture surface geometry can be systematically characterized through three key observations: (1) connecting the upper characteristic points with the rear anchor surface point delineates the primary rupture surface profile, (2) interpolation of the lower characteristic points defines the secondary rupture surface, and (3) the complete failure mechanism exhibits distinct geometric features—the upper surface develops at 35° with pronounced trumpet-shaped flaring, while the lower surface forms a steeper 40° arc that ultimately shears through to the free face (Figure 5). The location where a pronounced displacement shift occurs in the graph corresponds to the significant failure of the rock mass observed during the test. As indicated by the data, the most substantial displacement change is located at a depth of approximately 6 m in the monitoring borehole. This configuration demonstrates how stress redistribution progressively develops dual rupture surfaces with contrasting morphological characteristics under loading conditions.



(**a**) (**b**)

Figure 5. Inclinometer hole deformation trend. (**a**) Front anchorage face; (**b**) Rear anchorage face.

The failure mechanism analysis reveals two distinct zones: (1) a dislocation zone exhibiting tensile-shear failure dominance in its upper section transitioning to compressive-shear failure in the lower section, and (2) an adjacent disturbance zone showing progressive stress redistribution patterns. This zonal differentiation, illustrated in Figure 6, demonstrates the transition from tensile dominated to compression dominated failure modes along the depth gradient.

3.3. Test Results

Based on similar topographic and lithological conditions, a 1:12 in situ scale model test was conducted on a tunnel anchor in complex strata (conglomerate), including design load, multi-stage overload, failure, and creep tests. The results indicate: under design load, the deformation was largest at the free surface, followed by the front anchor surface, and smallest at the rear anchor surface; the relative dislocation between the anchor body and surrounding rock was most significant in the middle section; strain concentration was evident at the rear anchor surface. Deformation patterns under overload conditions were

consistent with those under design load. Failure tests revealed nonlinear rapid deformation growth between 8P and 10P load levels, suggesting an overload coefficient of 8P. Creep tests showed significant rheological behavior in the rock mass between anchors under 3.5P and 7P loads.

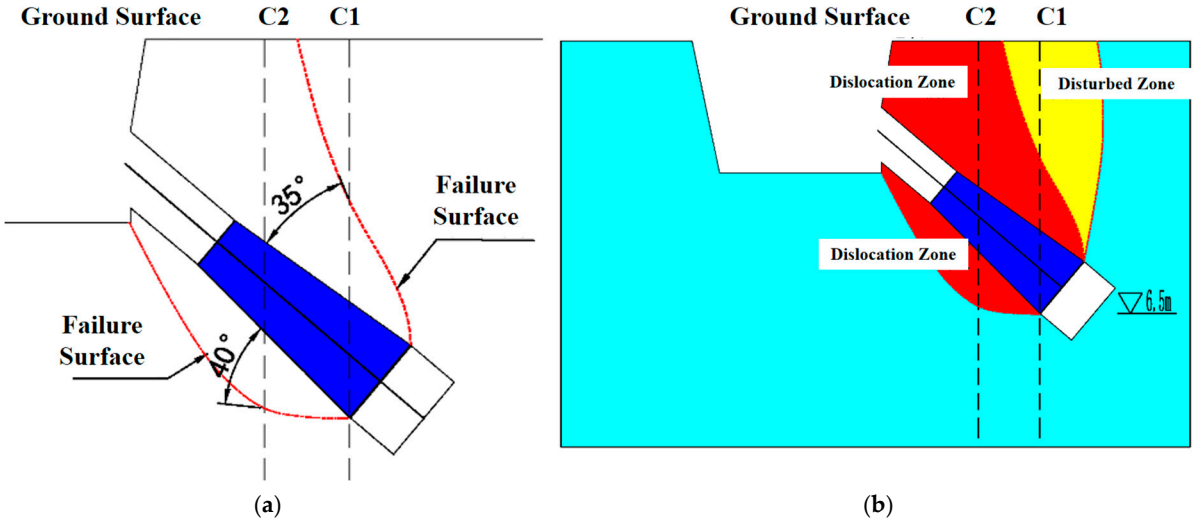


Figure 6. Model test results. (**a**) Generalized failure surface diagram; (**b**) Generalized zoning of surrounding rock failure.

4. Numerical Simulation

Through comprehensive on-site scaled model testing, this study establishes a reliable basis for calibrating three-dimensional numerical simulations, effectively eliminating potential scale effect distortions. Utilizing validated 3D numerical modeling techniques, the research systematically investigates the influence of multiple critical parameters including burial depth, installation angle, and overlying rock mass strength on the pullout stability characteristics and failure mechanisms of tunnel anchors.

4.1. Introduction to Numerical Simulation Method

FLAC 3D (Fast Lagrangian Analysis of Continua) is developed by the American company Itasca as an extension of the two-dimensional finite difference program FLAC 2D. It is capable of simulating the mechanical behavior and plastic flow of three-dimensional structures in soils, rocks, and other materials. The program adjusts polyhedral elements within the three-dimensional grid to fit actual structures. Element materials can adopt linear or nonlinear constitutive models. Under external forces, when materials yield and flow, the grid can correspondingly deform and move (large deformation mode).

The explicit Lagrangian algorithm and mixed-discrete partitioning technique employed by FLAC 3D enable highly accurate simulation of material plastic failure and flow. The mixed-discrete method, building upon classical discrete element methods, can simulate mixed-discrete phenomena in media. The mixed-discrete partitioning technique discretizes the computational domain by dividing the three-dimensional geological model into numerous sub-regions. All involved forces (applied and interactive) are concentrated at the nodes of the three-dimensional grid. Each polyhedral sub-region contains two superimposed sets composed of five tetrahedral sub-regions.

Within three-dimensional constant strain rate elements, tetrahedra offer the advantage of avoiding hourglass deformation—meaning deformation modes resulting from the combination of nodal velocities do not generate strain rates or nodal force increments. In the method proposed by Marti and Cundall, a coarser discretization within the region is superimposed onto the tetrahedral discretization. The first invariant of the strain rate for a specific tetrahedron in the region is calculated as the volumetric average of all tetrahedra in the region. This method is illustrated in Figure 7.

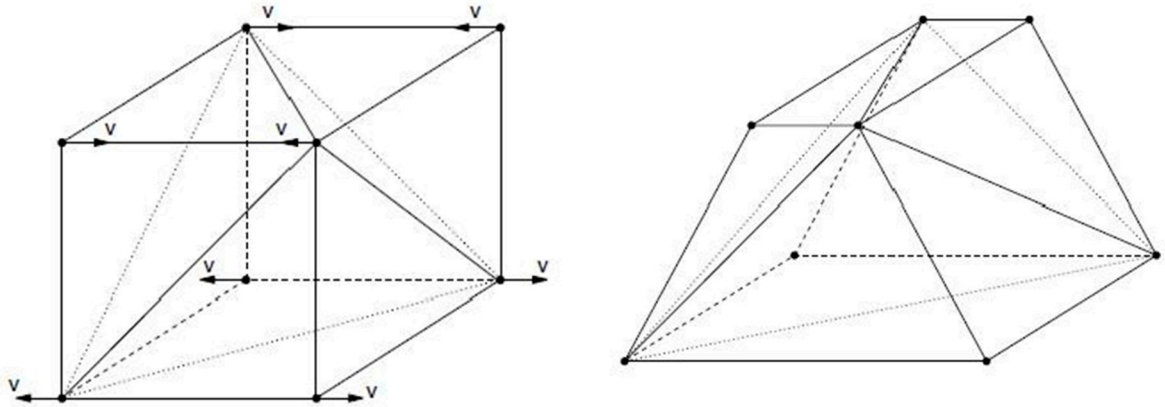


Figure 7. The most effective deformation mode of mixed discretization.

FLAC3D employs an explicit Lagrangian finite difference scheme to analyze the mechanical behavior of continuous three-dimensional media as it reaches equilibrium or steady plastic flow. It eliminates the need for iterative steps and does not require matrix formulation, overcoming limitations associated with small time steps and the need for damping through automatic inertial scaling and automatic damping. Simultaneously, assuming linear variations in variables over finite spatial and temporal intervals, it approximates the first-order spatial and temporal derivatives of the variables using finite differences.

The Fast Lagrangian Analysis method ultimately discretizes the medium into constant-strain-rate tetrahedral elements, where all involved forces (both applied and interactive) are concentrated at the vertices of the tetrahedra. These vertices serve as the nodes of the three-dimensional mesh. The finite difference formulation of the tetrahedral strain rate tensor components serves as a preliminary derivation for the nodal formulation of the equations of motion. The tetrahedron is illustrated in Figure 8.

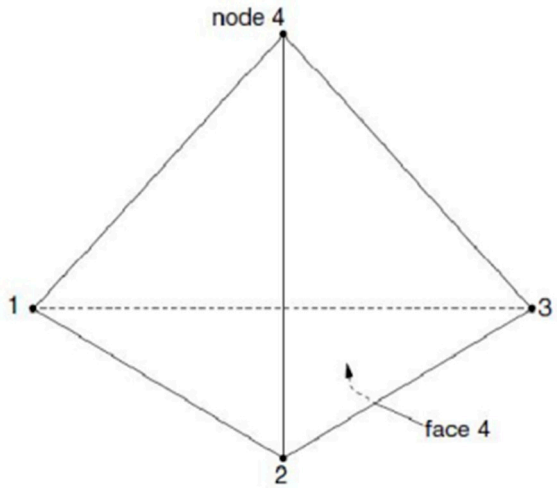


Figure 8. The Most Effective Deformation Mode in Mixed Discretization.

The four vertices of the tetrahedron are sequentially numbered from 1 to 4 as mesh nodes, with node n being opposite the corresponding face, designated as the n-th face of the tetrahedron. Assuming the velocity components at any point within the tetrahedron are v_i, applying the Gaussian divergence theorem to the tetrahedron and integrating over its volume and surface, respectively, the following expression can be formulated:

$$\int v_{ij} d_v = \int v_i n_j d_s \tag{1}$$

Here, v is the volume, s is the external surface, and n_j represents the component of the unit normal vector on the external surface. For a constant-strain-rate tetrahedron, the velocity field is linear and remains constant over each face. Consequently, after integration, Equation (2) yields:

$$v_{ij} = -\frac{1}{3v}\sum_{l=1}^{4} v_i n_j s \tag{2}$$

where the subscript l denotes the value associated with node l.

The computational principle of FLAC3D is as follows: The entire computational domain is discretized into multiple elements. After applying loads to the nodes of the elements, the equations of motion for the nodes are expressed in finite difference form. Based on the stress state at time t and the total strain increment over the time step Δt, the stress state at time t + Δt is determined. Using Gauss's theorem, the strain of an element is derived from the nodal velocities, and the element stress is computed via the corresponding stress–strain relationship. After integration, the stress vector at the nodes is obtained. Finally, the velocities and displacements of the nodes are solved through the equilibrium equations. This process is iterated until the entire computational domain reaches convergence, thereby accurately simulating the plastic failure and flow behavior of the material.

From the perspective of simulation command execution, FLAC3D can be systematically divided into three core components: model establishment, numerical simulation, and result output. The model establishment phase encompasses mesh generation, configuration of initial and boundary conditions, material parameter assignment, and initial stress equilibrium. The simulation phase involves load application and finite-difference-based solution of field equations. The output phase primarily comprises graphical visualization and data export functionalities.

The computational procedure of FLAC3D is as follows:

(1) Develop a three-dimensional geological model based on field survey data such as topographic contours and geological sections.
(2) Assign appropriate parameter values to the rock mass within the model.
(3) Apply boundary conditions and allow the model to reach equilibrium under its own gravitational load.
(4) Reset initial displacement states to zero and reassign parameters to the rock mass.
(5) Execute iterative calculations and analyze the resultant data.

4.2. Numerical Model and Numerical Simulation Setup

The coordinate system is defined with the bridge centerline as the *X*-axis (positive northward) and the vertical direction as the *Z*-axis (positive upward). The computational model, referenced to the bridge axis, spans 280 m longitudinally and 180 m laterally, with its base positioned at an elevation of −80 m. The model is shown in Figure 9. Based on model size requirements, computational efficiency, and solution accuracy considerations, the model was constructed with 1.45 to 1.70 million elements and 261,000 to 315,000 nodes.

The average length of the longest element edges ranges from 0.5 to 4.0 m, with a minimum edge length of 0.4 m. Mesh quality was controlled using smoothing techniques.

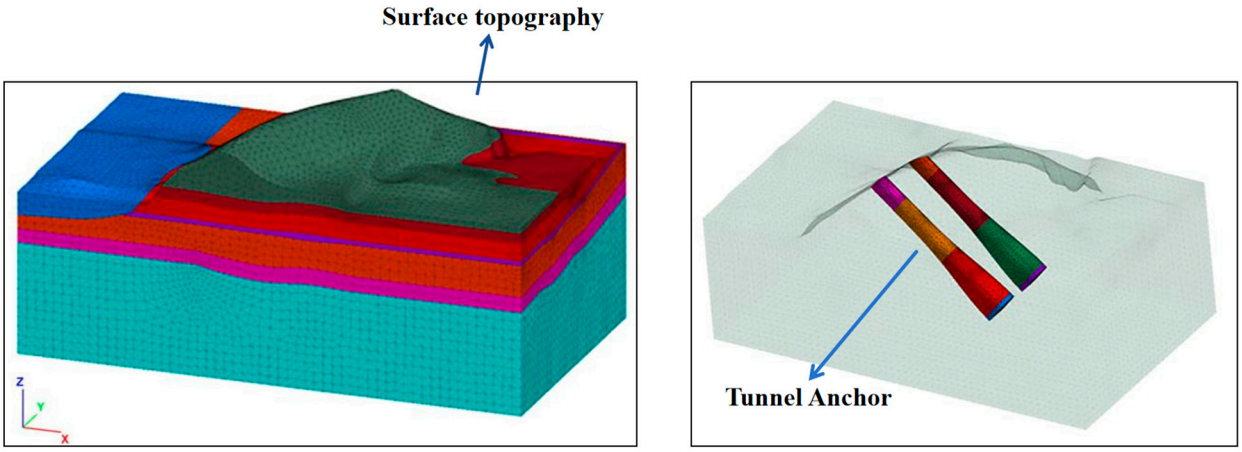


Figure 9. Numerical model. (**a**) Three-dimensional model; (**b**) Tunnel anchor layout.

In the FLAC3D finite difference software(FLAC3D 6.0 version), fixed displacement boundaries were applied at the model base to constrain vertical deformation. The left and right boundaries were constrained in the x-direction, while the front and rear boundaries were constrained in the y-direction. Initial in situ stresses were applied throughout the model volume, with gravitational loading being the primary source under these engineering conditions. Vertical stress was calculated based on gravitational forces, with horizontal stress set at 0.5 times the vertical stress. The applied stresses increased linearly with depth according to a defined gradient. The main cable load is applied as a distributed surface force on the posterior face of the concrete anchor block, with a design load magnitude of P = 220 MN. The rock mass is simulated with an elastoplastic Mohr-Coulomb constitutive model, whereas the anchor block's concrete material is modeled as linearly elastic.

4.3. Influence of Overlying Rock Mass Strength on Anchor Block Uplift Capacity

The tunnel anchor on the north bank of Wujiagang Yangtze River Bridge is principally embedded within the K_2l^1 stratum, which functions as the primary load-bearing layer. The overlying K_2l^2 and K_2l^3 strata, while not directly load-bearing, serve as critical overburden formations. Characterized by weak lithology, irregular thickness distribution, and substantial parameter heterogeneity, the Wujiagang tunnel anchor's overlying rock mass exhibits significant mechanical property variations. These geotechnical variations necessitate comprehensive investigation to evaluate their influence on the anchor system's pullout resistance performance.

A parametric study was conducted to evaluate the influence of overlying rock mass strength on tunnel anchor stability while maintaining constant geomechanical properties of the primary bearing stratum (K_2l^1). The investigation systematically reduced the overburden rock strength while keeping other parameters unchanged.

In a complementary analysis series, with fixed stratum thickness and consistent K_1l^1 rock mass parameters, the shear strength parameters of strata K_1l^{2-1} through K_1l^{2-5} and K_1l^3 were progressively reduced using reduction factors of 0.75 and 0.65, respectively. These sensitivity analyses were performed through advanced numerical modeling.

For all test scenarios, loading was applied in incremental stages until either structural failure was observed or the load reached 17 times the design load (17P), establishing ultimate capacity limits.

Monitoring points were strategically deployed in accordance with the three-dimensional geomechanical model test protocol, with specific instrumentation at four critical locations: (1) the front anchor surface, (2) the rear anchor surface, (3) the inter-anchor surrounding rock, and (4) the downstream-side surrounding rock. The spatial distribution of monitoring points maintains exact correspondence with the experimental model geometry, as documented in Figure 10. The circles in the diagram denote the locations and corresponding identification numbers of the monitoring points. They are positioned on the front anchorage face (upper section), the rear anchorage face (middle section), and the side of the tunnel anchor crown (lower section).

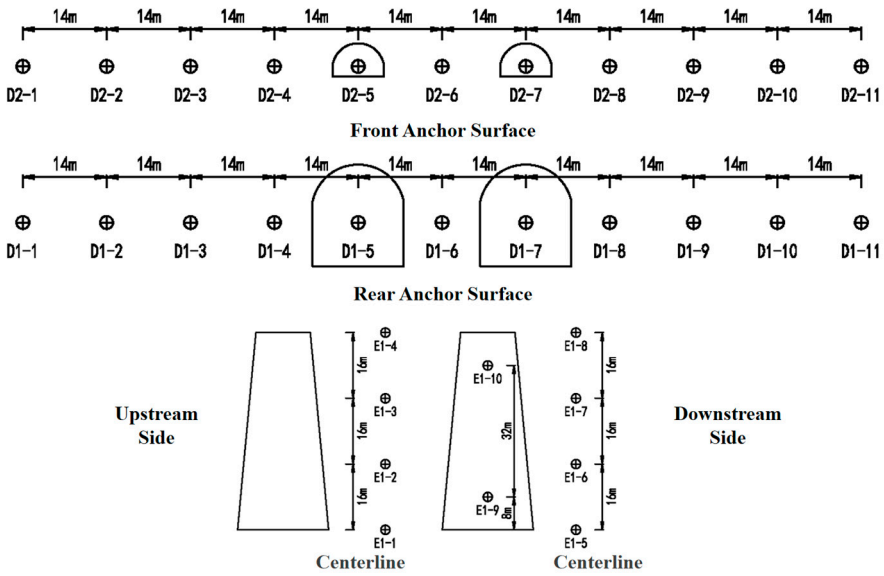


Figure 10. Internal monitoring points in rock mass and anchor body.

The load-plastic zone volume curves exhibit distinct inflection points in the evolution of tensile, shear, and total plastic failure volumes. As illustrated in Figure 11, both the actual ground condition and the 0.75 strength reduction scenario display nonlinear growth in plastic failure volumes once the applied load reaches 7P. If the abrupt expansion of plastic zones is used as the instability criterion for the tunnel anchor, the overload factors for both the in situ ground condition and the 0.75 strength reduction case reach 7.

A comparative analysis of the original stratum condition and the 0.75 strength reduction condition shows synchronous initiation of plastic zones in the main load-bearing rock mass. In both cases, plastic zones first develop in the upper rock mass behind the rear anchor face at 7P loading. However, their propagation behaviors differ significantly:

Under the 0.75 reduction condition, the plastic zone expands rapidly along the anchor-rock interface toward the front anchor face while developing bidirectionally between dual anchors, ultimately forming a penetrating failure zone at 13P loading.

In contrast, the original stratum condition displays more localized development, with the plastic zone initially expanding substantially in the top region behind the rear anchor face before gradually propagating toward the front anchor face.

These distinct propagation patterns clearly illustrate how rock mass parameter reduction influences the anchor's failure mechanism (see Figure 11).

The load-plastic zone volume relationship (Figure 11) demonstrates that under the 0.65 strength reduction condition, nonlinear growth initiates at a load of 5P. Using the onset of nonlinear plastic zone expansion as the instability criterion for the tunnel anchor yields a corresponding overload factor of 5.

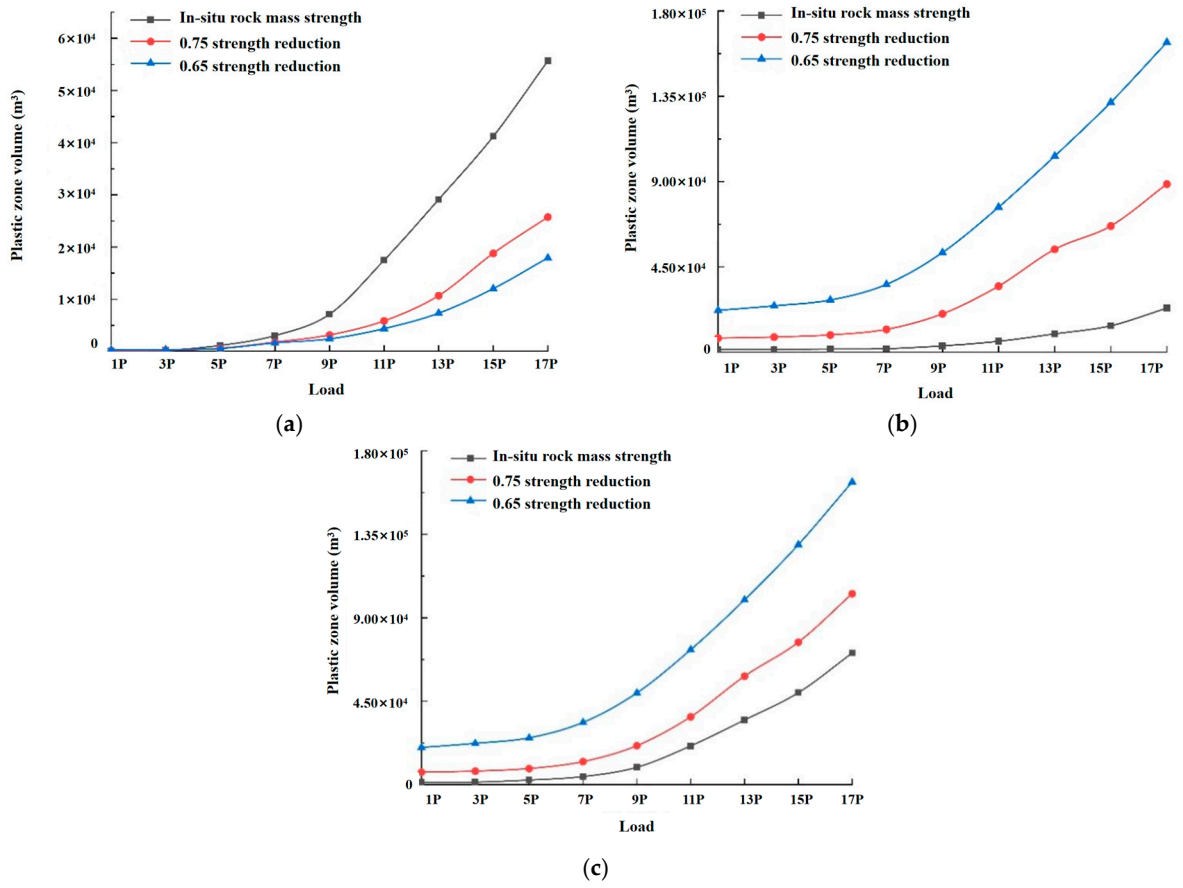


Figure 11. Load-plastic zone volume evolution curve. (**a**) Tension-shear failure; (**b**) Shear failure; (**c**) Total plastic zone volume.

Comparative analysis shows the critical load for abrupt plastic zone expansion in the 0.65 reduction case occurs at significantly lower loading levels compared to the 0.75 reduction scenario. This behavior difference principally arises from excessive plastic deformation developing along the anchor tunnel walls when the overlying rock mass strength proves inadequate to resist the applied stresses.

4.4. Effect of Installation Angle on Anchor Pullout Capacity

The installation angle of a tunnel anchor is defined as the inclination angle between the anchor axis and the horizontal plane. In tunnel anchor design, the steel strands anchored to the structure must converge precisely at the splay saddle to form the main cable without dispersion, requiring careful adjustment of the installation angle to ensure proper cable constraint forces at the saddle.

To evaluate the effect of installation angle on pullout resistance, a series of numerical simulations were performed under in situ geological conditions. Five installation angles were investigated: 35°, 37.5°, 40° (design condition), 42.5°, and 45°, systematically analyzing their influence on anchor performance.

To enable controlled comparative analysis while eliminating confounding effects from burial depth and lithological variations, the tunnel anchor's geometric dimensions were held constant, with the center point of the rear anchor face designated as the rotational reference. Numerical simulations were conducted by incrementally rotating the anchor to specified angles while applying progressively increasing loads until either structural failure initiation or attainment of 17 times the design load (17P) was achieved. The complete simulation setup is presented in Figure 12.

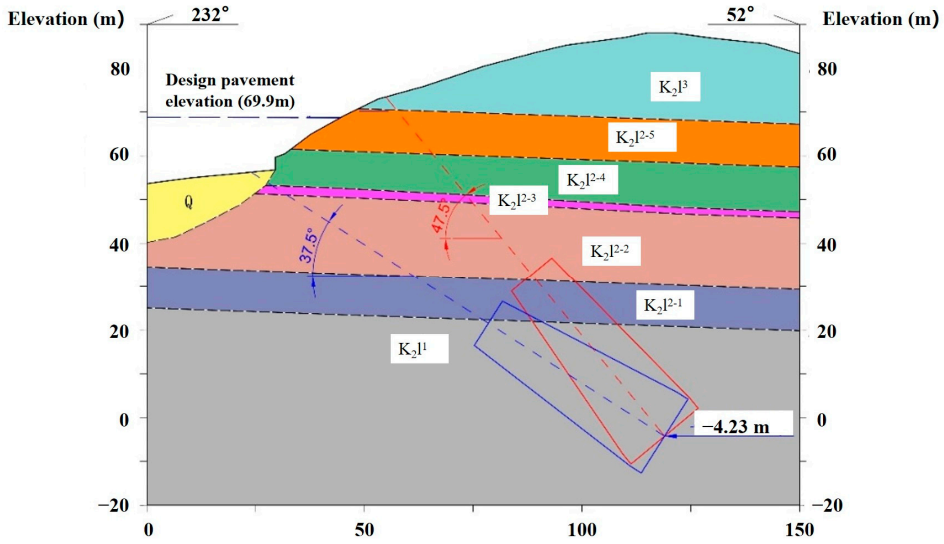


Figure 12. Different installation angles of tunnel anchor.

Numerical simulation results (Figure 13) reveal that although varying installation angles (35–45°) exert limited effects on the initial distribution and overall development trends of plastic zones in the load-bearing rock mass-with all cases exhibiting synchronous plastic zone initiation at the rear anchor vault and inter-anchor sidewalls under 7P loading they markedly alter the penetration rate. Notably, the 45° installation angle demonstrates the most rapid vault-to-front penetration, followed by 35°, whereas the designed 40° configuration shows the slowest progression. Crucially, all cases develop plastic zones similarly in the inter-anchor rock mass, achieving complete penetration uniformly at 17P loading, with failure surfaces evenly distributed across inter-anchor zones, the crown vault, and perimeter sidewalls. These results indicate that while the installation angle modulates the rate of local failure progression, it scarcely affects the ultimate failure mode.

4.5. Effect of Burial Depth on Anchor Pullout Capacity

To examine the effect of burial depth on the pullout resistance of tunnel anchors, a sequence of numerical simulations was performed with invariant anchor geometry. Using the elevation of the bottom edge of the rear anchor face as a reference, seven burial depth conditions were evaluated by vertically displacing the anchor in ±10 m increments. The resulting elevations of the rear anchor face bottom edge were −41.9 m, −31.9 m, −21.9 m, −11.9 m, −1.9 m, 8.1 m, and 18.1 m, respectively (see Figure 14). In each numerical model, progressive loading was applied from the rear anchor face until either structural failure initiated or a load of 17 times the design value (17P) was attained.

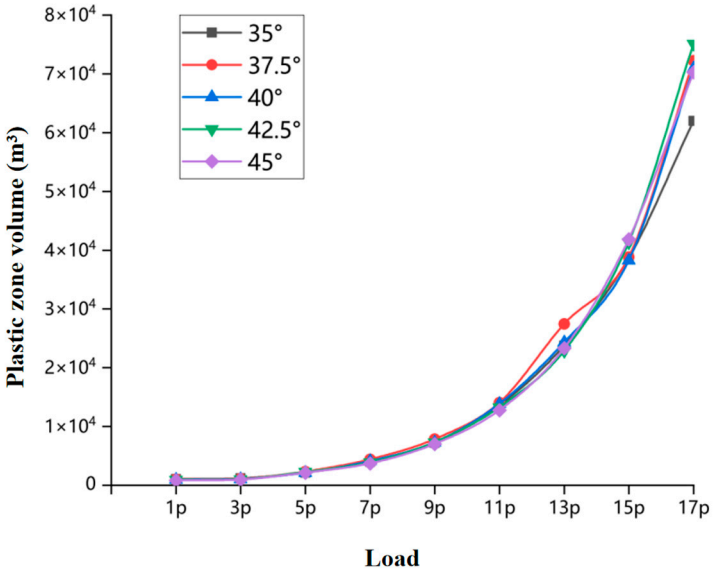


Figure 13. Plastic zone volume versus load variation under different installation angles of tunnel anchor.

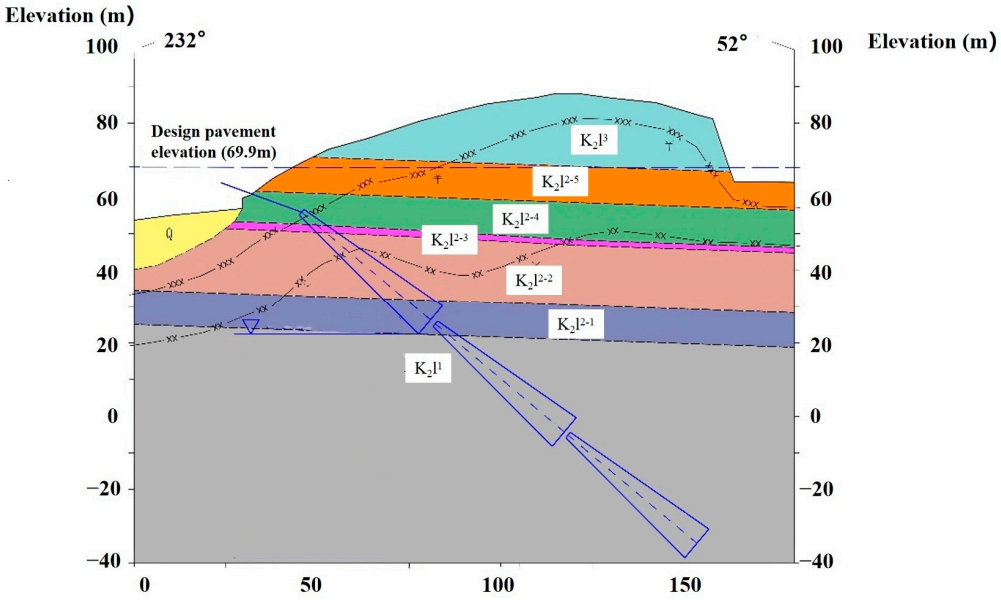


Figure 14. Different burial depths of tunnel anchors.

Analysis of the load-plastic zone volume relationships (Figure 15) reveals a distinct depth-dependent pattern in plastic zone evolution: shallow-depth anchors (elevations −1.9 m, 8.1 m, and 18.1 m) initiate nonlinear growth at relatively low load levels (3–5P), whereas intermediate-depth anchors (−21.9 m and −11.9 m) exhibit this transition at higher loads (5–7P). Notably, deep burial cases (−41.9 m and −31.9 m) show no discernible inflection points, indicating substantial suppression of plastic zone development. These results collectively demonstrate that increased burial depth enhances confining pressure, progressively restraining plastic zone propagation in the surrounding rock mass. Specifically, shallow cases develop early nonlinearity at 3–5P, intermediate cases resist deformation until 5–7P, and deep anchors maintain notable stability throughout the loading process.

Analysis of plastic zone initiation and progression across varying burial depths reveals a significant positive correlation: greater depths require substantially higher loads to initiate plastic deformation. This behavior is attributed to enhanced confining pressure in the surrounding rock at increased depths, which elevates the threshold load required

for rock mass failure. The results demonstrate that deeper burial conditions effectively restrain plastic zone penetration, suggesting that beyond a critical depth, the surrounding rock develops adequate strength to significantly enhance the clamping capacity of the load-bearing stratum. Under such conditions, even applied loads considerably higher than the design load induce only gradual plastic failure within the bearing stratum, rendering sudden instability highly improbable.

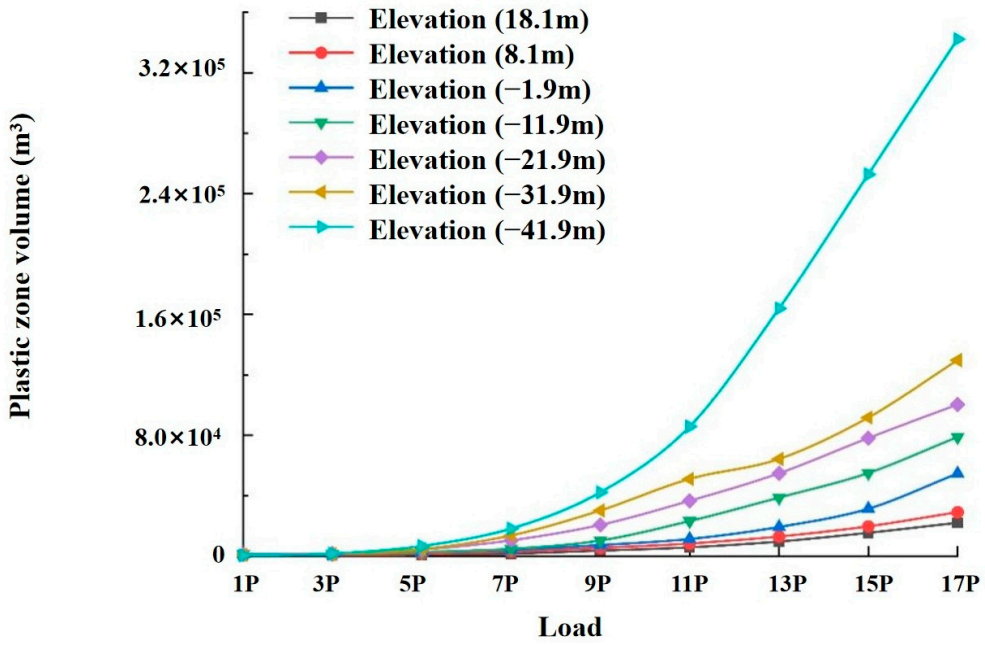


Figure 15. Variation in total plastic volume of tunnel anchors at different burial depths.

4.6. Stability and Potential Failure Modes of Tunnel Anchor

4.6.1. Excavation-Induced Deformation

Figure 16 illustrates the distribution of the plastic zone following excavation. The results indicate that tunnel excavation induces stress redistribution, resulting in a progressive expansion of the plastic zone in the surrounding rock as excavation advance and cross-sectional dimensions increase. Notably, when the tunnel section transitions to a variable diameter, the plastic zone exhibits significant amplification while remaining non-penetrating through the central diaphragm. In Figure 16a,b, the green color indicates the undeformed zones. The red and pink zones represent areas of tensile and shear deformation, which are mainly confined to the vicinity of the tunnel anchors. The fact that these deformed zones are not interconnected between the two anchors suggests that no failure has developed. As shown in the 3D plastic zone distribution of Figure 16c, the plasticity is likewise distributed only around the anchors, with no continuous failure surface forming internally.

Figure 17 presents the post-excavation displacement field. The results demonstrate that tunnel excavation causes significant deformation in the surrounding rock, with displacement magnitudes escalating proportionally to cross-sectional size. The maximum deformation occurs at about 2/3 of the tunnel length, where crown settlement peaks at 11.1 mm and sidewall convergence reaches 5.4 mm.

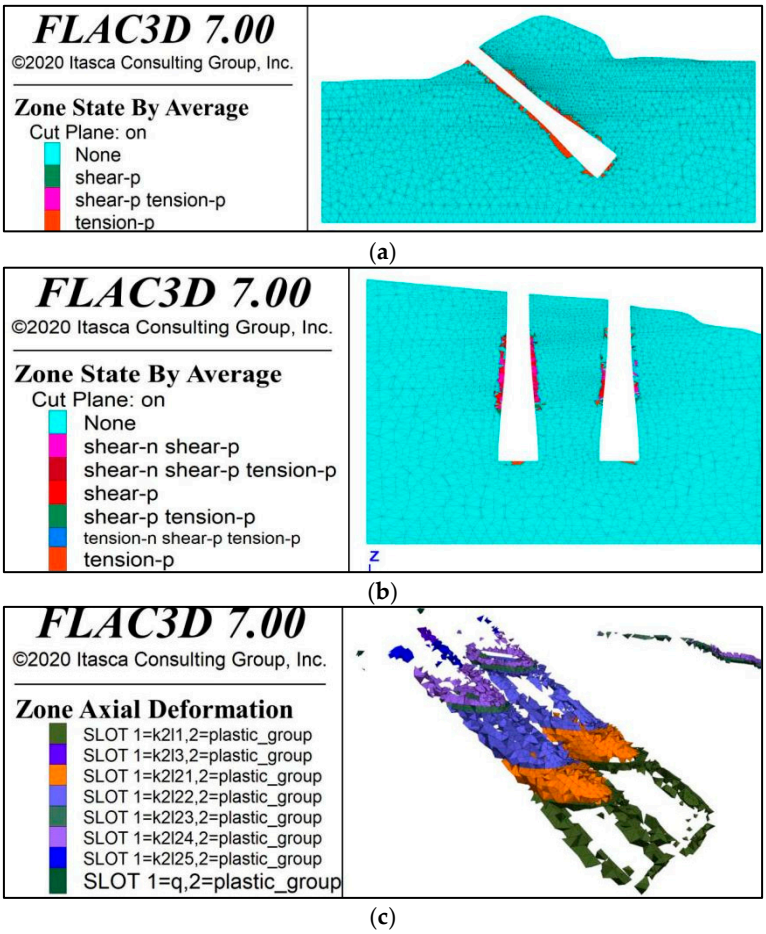
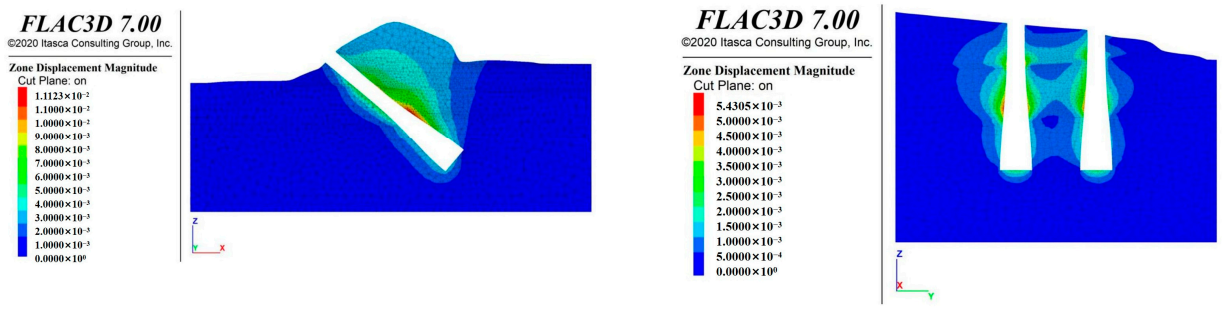


Figure 16. Excavation-induced plastic zone in the model. (**a**) Front view; (**b**) Profile view; (**c**) 3D view.



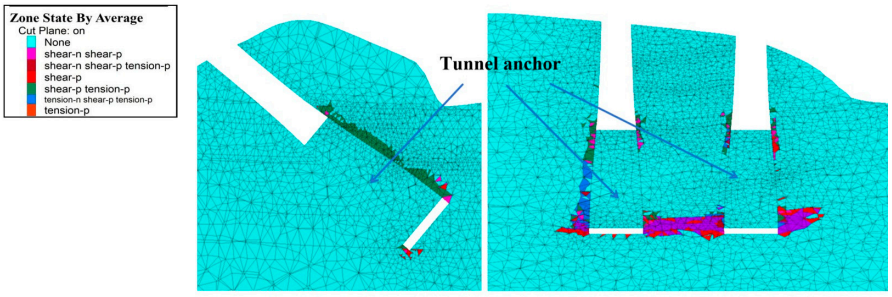
(**a**) (**b**)

Figure 17. Excavation-induced displacement in the model. (**a**) Front view; (**b**) Profile view.

4.6.2. Potential Failure Modes

1. Failure modes

Shallow Failure: At shallow burial depths, the applied load transmits to the ground surface, often leading to overall pullout failure of the overlying rock mass (Figure 18). The process is characterized by the expansion of the plastic zone from the rear anchor surface upward until it breaks through to the ground, consistent with observations from physical model tests.



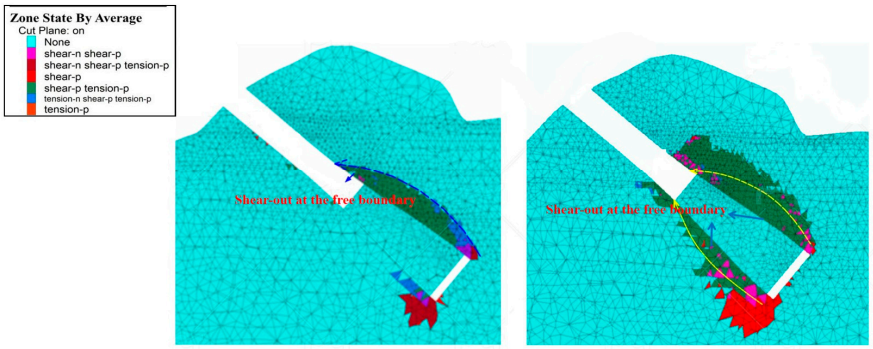
(**a**) (**b**)

Figure 18. Plastic zone penetration. (**a**) Profile view; (**b**) Front view.

Deep Failure: Under larger burial depths (ranging from −11.9 m to −41.9 m), ground surface deformation is negligible. Failure in such cases occurs through full plastic penetration within the bearing layer and can be categorized into two modes:

(1) Double Shear-Out Failure: At moderately deep positions within this range, the plastic zone shears out bilaterally toward the free boundary near the front anchor (Figure 19a).

(2) Single Shear-Out Failure: At greater depths, the plastic zone propagates from the rear anchor surface and shears out unilaterally toward the front anchor face (Figure 19b).



(**a**) (**b**)

Figure 19. Failure modes. (**a**) Deep single shear-out failure mode; (**b**) Deep double shear-out failure mode).

Shallow failure is governed by the shear strength of the overburden rock, while deep failure depends on the strength of the bearing layer and the surrounding confining pressure. Increasing the burial depth does not change the fundamental failure mode.

2. Stability analysis

Under the 1P design load, the anchorage system remains stable, with measured deformations of 0.4 mm and 0.7 mm at the front and rear anchor faces, respectively (Figure 20). The structural health is further demonstrated by the elastic state of the bearing layer. While sporadic plastic zones are locally present at the crown of the front anchorage face, no plasticity is observed in the surrounding rock of the load-bearing stratum. This confirms that the entire anchorage is in a stable and sound condition.

Overload Condition: The overload coefficient reaches 12P when the plastic zone fully penetrates (as per numerical simulation). However, considering reduced-scale test results (8P–9P) and overall engineering safety, a value of 8P is adopted as the design overload threshold (Figure 21).

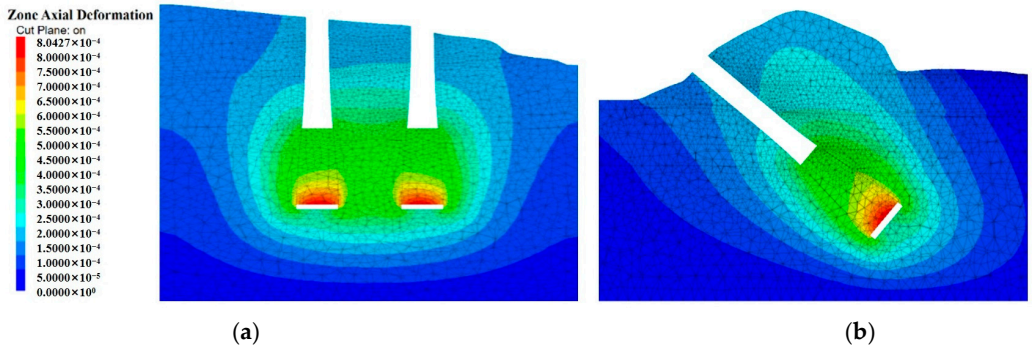


Figure 20. Displacement under design load. (**a**) Front view; (**b**) Profile view.

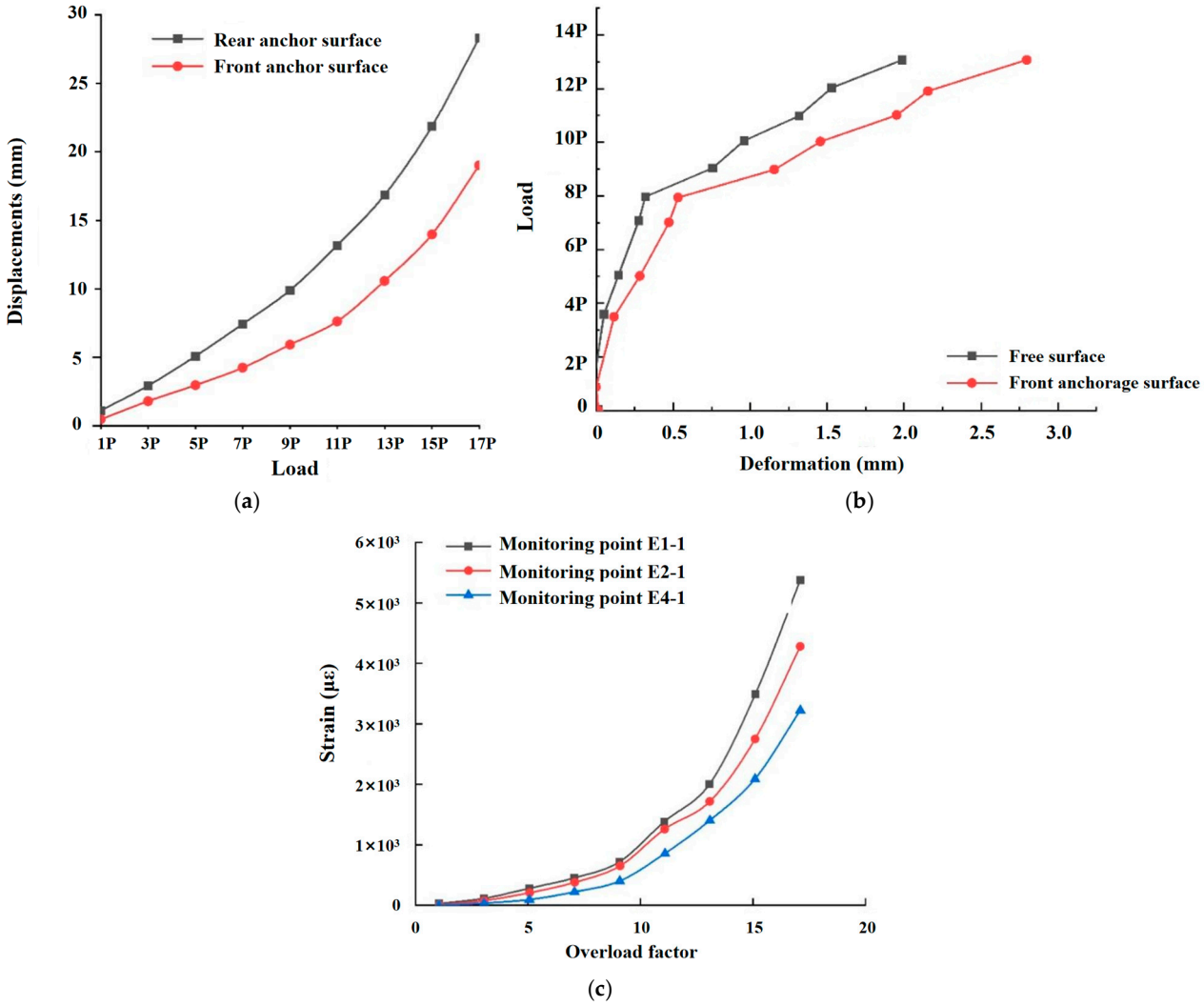


Figure 21. Overload tests. (**a**) Monitoring points displacement; (**b**) Deformation of surrounding rock between anchors under graded loads; (**c**) Overload deformation of the monitoring points between anchors).

3. Long-term creep (1P, 24 months)

Displacement increased during the initial stage and stabilized after 15 months, with the maximum value remaining below 3.5 mm-well under the allowable limit of 190 mm specified by the design code (Figure 22).

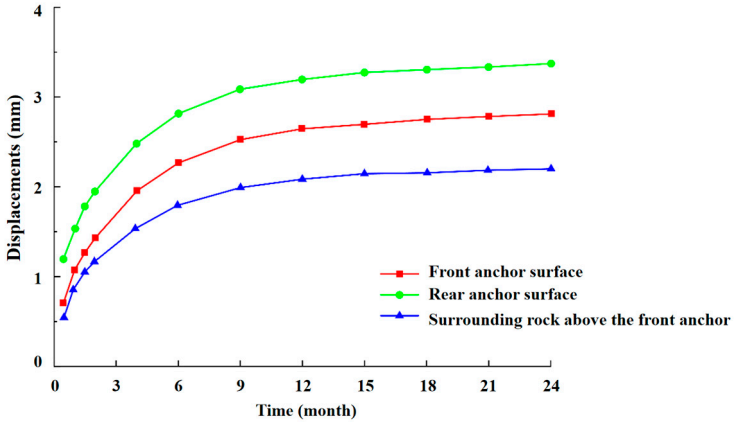


Figure 22. Creep under design load.

The plastic zone is limited to the area adjacent to the anchorage end face, demonstrating favorable long-term stability (Figure 23). The tunnel anchorage of Wujiagang Bridge exhibits adequate stability under both shallow and deep failure modes. The design load and long-term creep performance meet all safety requirements, with a conservatively selected overload coefficient of 8P.

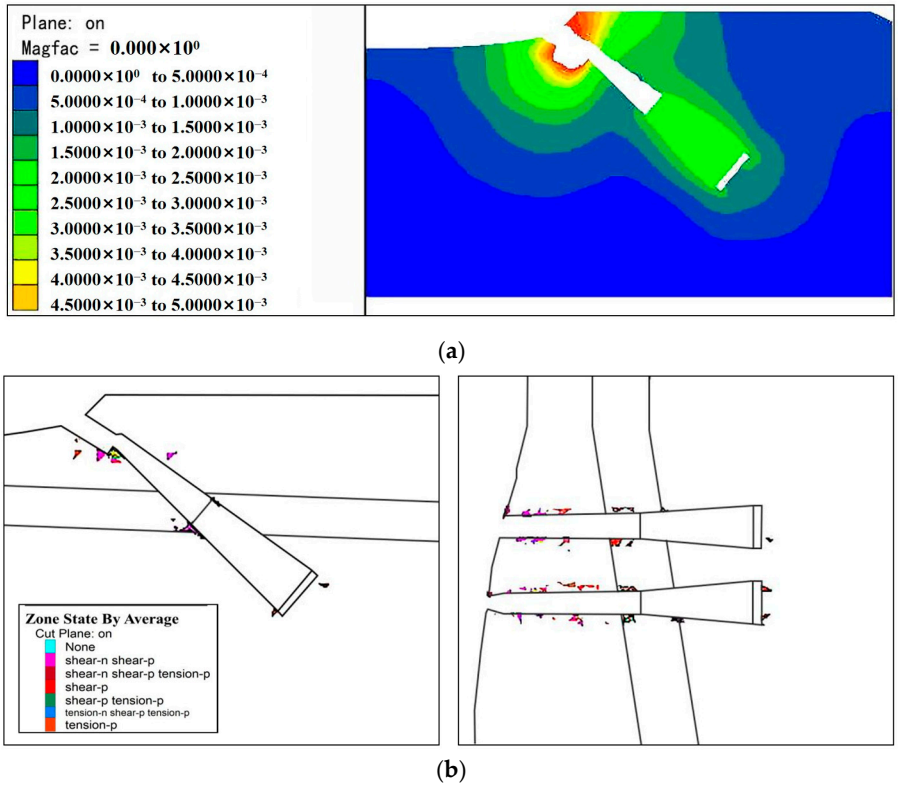


Figure 23. Characteristics of surrounding rock under design load over 24 months. (**a**) Displacement; (**b**) Plastic zone.

The 3D numerical simulation results show general agreement with physical test data, revealing a pronounced tensile-shear slip tendency between the twin anchors that may lead to plastic connectivity failure. The comprehensive 3D analysis further identifies potential risks of plastic zone penetration at the anchor crown and both sidewalls.

5. Conclusions

This study is based on the Wujiagang Yangtze River Bridge project in Yichang, with a focus on the tunnel anchorage at the north bank. Building upon laboratory rock physico-mechanical tests and in situ rock mass mechanical tests, model tests were conducted at different scales, both in the laboratory and on site. Through theoretical analysis, machine learning, and numerical calculations, systematic and in-depth research was carried out on the pullout mechanism, failure modes, and long-term stability of the tunnel anchorage. The main conclusions are as follows:

(1) Based on a 1:12 scaled field model test, results of surrounding rock deformation, strain, and creep under 1P (design load), 3.5P, 7P, and destructive test conditions were obtained. Under different load levels, the maximum deformation occurred at the free surface, followed by the front anchor face, with the smallest deformation at the rear anchor face. The relative deformation between the anchorage and surrounding rock was greatest in the middle part of the anchor body, followed by the rear anchor face, and smallest at the front anchor face. The strain was highest at the rear anchor face, moderate in the middle part, and smallest at the front anchor face, with a significant difference in deformation between the front and rear anchor faces. The rheological characteristics of the rock mass between the two anchors were not significant under 1P load but became evident under 3.5P and 7P loads.

(2) Based on a 1:1 three-dimensional numerical simulation, the influence of overlying rock mass strength on the pullout capacity of the tunnel anchorage was studied. It was found that the strength of the overlying rock mass has a weak influence on the tunnel anchorage. It revealed that the pullout capacity of the tunnel anchorage is primarily determined by the strength of the bearing layer rock mass. The influence range of the bearing layer is consistent with the results of the three-dimensional geomechanical model test, ranging from 1 to 2 times the width of the rear anchor face, and this range varies little under different lithologies and burial depths.

(3) Based on numerical simulation, five installation angle conditions were studied. The results showed that the deformation of the surrounding rock, the expansion of the plastic zone, and the overload capacity were generally consistent under different installation angles. This reveals that under the same stratum and burial depth conditions, the installation angle of the tunnel anchorage has little effect on its pullout capacity.

(4) Based on numerical simulation, seven burial depth conditions were studied. It was found that increasing the burial depth can improve the pullout capacity of the tunnel anchorage, but the effect is limited when the bearing layer remains the same. The burial depth selected for the Wujiagang Bridge is appropriate.

Author Contributions: Conceptualization, M.D.; Methodology, Z.S.; Software, L.Z.; Validation, M.D. and A.T.; Formal analysis, X.G. and A.T.; Investigation, Z.S., X.G., L.Z. and A.T.; Resources, Z.S., X.G. and A.T.; Data curation, X.G. and L.Z.; Writing—original draft, M.D.; Writing—review & editing, L.Z.; Supervision, Z.S.; Project administration, M.D. All authors have read and agreed to the published version of the manuscript.

Funding: This research received no external funding.

Institutional Review Board Statement: Not applicable.

Informed Consent Statement: Not applicable.

Data Availability Statement: The original contributions presented in this study are included in the article. Further inquiries can be directed to the corresponding author.

Conflicts of Interest: Authors Zhijin Shen, Geng Xiaojie, Li Zhang and Aipeng Tang were employed by the company Changjiang Survey, Planning, Design and Research Co., Ltd. The remaining author declares that the research was conducted in the absence of any commercial or financial relationships that could be construed as a potential conflict of interest.

References

1. Liu, B.; Ma, J.; Wang, L.; Chen, J.G.; Chen, K.L. Overall Design of Jin'an Jinsha River Bridge in Yunnan. *Bridge Constr.* **2018**, *48*, 82–87.
2. Hu, J.H.; Cui, J.F. Innovative Techniques of Design ofsss Aizhai Bridge in West Hunan. *Bridge Constr.* **2011**, *6*, 54–61. [CrossRef]
3. Wang, H.B.; Gao, B.; Sun, Z. Study on the Mechanical Behaviour of Tunnel Anchorage Systems for Suspension Bridges. *Chin. J. Rock. Mech. Eng.* **2005**, *24*, 2728–2735. [CrossRef]
4. Jung, M.R.; Zhang, F.; Kim, M.Y. Extended Deflection Theories of Self-anchored Suspension Bridges with Extensible Hangers and Floating Girders. *KSCE J. Civ. Eng.* **2024**, *28*, 3928–3940. [CrossRef]
5. Li, R.; Zhou, J.; Qin, Q.; Yuan, S.; Cui, K.; Yue, F.; Song, S.; Xue, Z. Study of the static response and zoning of the existing tunnel adjacent to the suspension bridge's tunnel-type anchorage. *Sci. Rep.* **2024**, *14*, 21402. [CrossRef]
6. Jiang, N.; Wang, D.; Feng, J.; Zhang, S.L.; Huang, L. Bearing mechanism of a tunnel-type anchorage in a railway suspension bridge. *J. Mt. Sci.* **2021**, *18*, 2143–2158. [CrossRef]
7. Li, D.; Liu, X.; Wu, X.; Li, W. Three-Dimensional Elastoplastic Analysis on the Stability of Tunnel Anchorage in Soft Rock. In Proceedings of the 4th Geo-China International Conference on Sustainable Civil Infrastructures-Innovative Technologies, Jinan, China, 25–27 July 2016. [CrossRef]
8. Cao, C.M.; Yi, L.X.; Wang, B.B. Design and Study of Tunnel Anchorage for Wujiagang Changjiang River Bridge in Yichang. *Bridge Constr.* **2020**, *50*, 80–85.
9. Jiang, B.; Wu, K.B.; Wang, Q.; Wang, Y.; Li, D.; Deng, Y. High prestressed anchorage support for tunnel surrounding rock model test method and its control effect. *Tunn. Undergr. Space Technol.* **2025**, *157*, 106332. [CrossRef]
10. Dai, M.J.; Zhou, C.D.; Zeng, D.L. Field Scaled Model Test of Tunnel Anchorage of Wujiagang Changjiang River Bridge Socketed in Soft Rock. *Bridge Constr.* **2021**, *51*, 68–75. [CrossRef]
11. Mao, D.W.; Du, S.H.; Zuo, C.G.; Mei, S.H. Experimental study on bearing characteristics of in-situ model of tunnel-type anchorage for a suspension bridge under different scales. *J. Railw. Sci. Eng.* **2024**, *21*, 2384–2395. [CrossRef]
12. Yu, M.W.; Zhang, Q.H.; Gao, L.P.; Luo, R.; Li, Y.J.; Wang, S.; Bian, Z.H. Field model tests and bearing capacity analysis of tunnel anchorage of Jindong Bridge. *Chin. J. Geotech. Eng.* **2021**, *43*, 338–346. [CrossRef]
13. Liu, X.R.; Han, Y.F.; Jing, R.; Li, D.L.; Tu, Y.L. Bearing Characteristics, Deformation Failure Characteristics and Typical Case Studies of Tunnel-type Anchorage. *Chin. J. Undergr. Space Eng.* **2019**, *15*, 1780–1791.
14. Wang, G.; Zheng, C.C.; Jiang, F.; Yuan, W.; He, P.; Xiao, Z. Analysis of elastic and rheological properties of tunnel anchorage support structure under the action of seepage flow. *Sci. Rep.* **2024**, *14*, 29030. [CrossRef]
15. Wu, A.; Zhang, Y.; Luo, R.; Xu, D.; Fan, L.; Zhou, H.; Wu, X.; Wu, Y.; Li, Y. A Field Model Test Method of Tunnel-Type Anchorages in Rock Mass and Its Application in Railway Suspension Bridge Engineering. *Rock Mech. Rock Eng.* **2023**, *56*, 8891–8906. [CrossRef]
16. Han, Y.F.; Liu, X.R.; Wei, N.; Li, D.; Deng, Z.; Wu, X.; Liu, D. Comprehensive Review of the Mechanical Behavior of Suspension Bridge Tunnel-Type Anchorage. *Adv. Mater. Sci. Eng.* **2019**, *2019*, 3829281. [CrossRef]
17. Han, Y.F.; Liu, X.R.; Li, D.L.; Tu, Y.; Deng, Z.; Liu, D.; Wu, X. Model test on the bearing behaviors of the tunnel-type anchorage in soft rock with underlying weak interlayers. *Bull. Eng. Geol. Environ.* **2020**, *79*, 1023–1040. [CrossRef]
18. Shen, Z.J.; Jia, J.H.; Jiang, N.; Zhu, B.; Sun, W. Field-Scale Experiment on Deformation Characteristics and Bearing Capacity of Tunnel-Type Anchorage of Suspension Bridge. *Energies* **2022**, *15*, 4772. [CrossRef]
19. Lim, H.; Seo, S.; Lee, S.; Chung, M. Analysis of the passive earth pressure on a gravity-type anchorage for a suspension bridge. *Int. J. Geo-Eng.* **2020**, *48*, 1545–1551+1587. [CrossRef]
20. Lim, H.; Seo, S.; Ko, Y.H.; Lee, S.; Chung, M. Analysis of Failure Mode on Tunnel-Type Anchorage by Model Tests and Numerical Analyses. *Int. Found. Congr. Equip. Expo* **2021**, *325*, 217–226.
21. Seo, S.; Lim, H.; Chung, M. Evaluation of failure mode of tunnel-type anchorage for a suspension bridge via scaled model tests and image processing. *Geomech. Eng.* **2021**, *24*, 457–470. [CrossRef]
22. Xia, Z.G.; Ma, C.L.; Yin, D.W.; Wang, C.; Jiang, N.; Zhang, X. Influence of confining pressure and structural plane inclination on rock interface slip. *Phys. Fluids* **2025**, *37*, 041909. [CrossRef]
23. Liang, N.H.; Han, Y.F.; Xiao, Y.; Liu, X.; Zhou, X. Settlement Law of Overlying Plug Body Caused by Close Construction of Underpass Tunnel Anchorage. *Chin. J. Undergr. Space Eng.* **2023**, *19*, 1938–1947.
24. Zhou, X.H.; Liu, X.R.; Xiao, Y.; Liang, N.; Yang, Y.; Han, Y.; Yang, Z. Analysis of stability control and the adapted ways for building tunnel anchors and a down-passing tunnel. *Geomech. Eng.* **2023**, *35*, 395–409. [CrossRef]

25. Zhang, J.; Ma, J.L.; Wang, Q.K.; Wei, S. Stability of Tunnel Anchorage of Long-span Suspension Bridge in Fractured Rock Interlayer. *J. Yangtze River Sci. Res. Inst.* **2024**, *41*, 149–156. [CrossRef]
26. Ko, J.; Lim, H.; Seo, S.; Chung, M. Assessment of pull-out behavior of tunnel-type anchorages under various joint conditions. *Geomech. Eng.* **2024**, *36*, 71–81. [CrossRef]
27. Thirukumaran, S.; Oliveira, D.; Ariza, L. Assessing the Relative Quality of Rock Bolt Grouting in Weak Rock Mass Based on In Situ and Numerical Pull-Out Tests. *Rock Mech. Roc. Eng.* **2025**, *58*, 10497–10522. [CrossRef]
28. Sahoo, J.P.; Kumar, J. Stability of a circular tunnel in presence of pseudostatic seismic body forces. *Tunn. Undergr. Space Technol.* **2014**, *42*, 264–276. [CrossRef]

Disclaimer/Publisher's Note: The statements, opinions and data contained in all publications are solely those of the individual author(s) and contributor(s) and not of MDPI and/or the editor(s). MDPI and/or the editor(s) disclaim responsibility for any injury to people or property resulting from any ideas, methods, instructions or products referred to in the content.